OPTICA

High-fidelity ptychographic imaging of highly periodic structures enabled by vortex high harmonic beams

Bin Wang,[1],[†],[*] Nathan J. Brooks,[1],[†] Peter Johnsen,[1] Nicholas W. Jenkins,[1] Yuka Esashi,[1] Iona Binnie,[1] Michael Tanksalvala,[1] Henry C. Kapteyn,[1],[2] and Margaret M. Murnane[1]

[1]*STROBE Science and Technology Center, JILA, University of Colorado, Boulder, Colorado 80309, USA*
[2]*KMLabs Inc., 4775 Walnut St. #102, Boulder, Colorado 80301, USA*
[†]*These authors contributed equally to this work.*
[*]*bin.wang-2@colorado.edu*

Ptychographic coherent diffractive imaging enables diffraction-limited imaging of nanoscale structures at extreme ultraviolet and x-ray wavelengths, where high-quality image-forming optics are not available. However, its reliance on a set of diverse diffraction patterns makes it challenging to use ptychography to image highly periodic samples, limiting its application to defect inspection for electronic and photonic devices. Here, we use a vortex high harmonic light beam driven by a laser carrying orbital angular momentum to implement extreme ultraviolet ptychographic imaging of highly periodic samples with high fidelity and reliability. We also demonstrate, for the first time to our knowledge, ptychographic imaging of an isolated, near-diffraction-limited defect in an otherwise periodic sample using vortex high harmonic beams. This enhanced metrology technique can enable high-fidelity imaging and inspection of highly periodic structures for next-generation nano, energy, photonic, and quantum devices.   © 2023 Optica Publishing Group under the terms of the Optica Open Access Publishing Agreement

https://doi.org/10.1364/OPTICA.498619

1. INTRODUCTION

In recent decades, a powerful coherent diffractive imaging (CDI) technique known as ptychography has enabled robust, diffraction-limited, phase-contrast imaging of nanoscale structures [1–5]. Although ptychography has been implemented using a range of illumination wavelengths, its use in the extreme-ultraviolet (EUV) and x-ray regions is particularly attractive for achieving high spatial resolution with inherent elemental and chemical contrast [6–10]. In ptychography, a coherent illumination (the probe) is focused and scanned across an extended sample. A series of far-field diffraction patterns are recorded, while maintaining a large overlap between adjacent scan positions. Iterative phase-retrieval algorithms [11–15] can then be used to robustly and uniquely reconstruct the complex-valued probe field and sample transmission or reflection functions. However, successful reconstruction relies heavily on diversity in the data provided by the lateral scanning of the probe relative to the sample, i.e., interferences at the detector plane mix amplitude and phase, allowing the reconstruction algorithms to unravel both. This means that ptychographic imaging of highly periodic samples with a sufficiently small period is extremely challenging due to the lack of diversity in a series of diffraction patterns, leading to poor convergence of the reconstructed sample images. This significantly limits ptychography's

application to a wide variety of nanoscale periodic structures such as photonic crystals [16,17], semiconductor devices [18], and EUV photomasks [19–25]. Consequently, it is critical to fill this characterization gap to aid the advancement of a host of next-generation nano-devices.

High harmonic upconversion of femtosecond lasers can produce bright coherent beams from the EUV to the soft x-ray regions of the spectrum in a tabletop-scale setup [26–28]. When combined with ptychography, high harmonic generation (HHG) enables phase-sensitive lensless imaging with diffraction-limited nanoscale spatial resolution and excellent elemental specificity [9,15,29–31]. Moreover, because of the quantum-coherent nature of the HHG upconversion process, polarization and phase structure present in the driving laser beam can be transferred to the generated harmonics, provided energy, spin, and orbital angular momentum are conserved [32,33]. This makes it possible to create designer short-wavelength structured light for a variety of applications in advanced spectro-microscopies [34,35].

Past work has shown that the structure of the illumination beam plays a significant role in image quality and even spatial resolution in ptychography [31,36–42]. For example, light beams carrying orbital angular momentum (OAM) have attracted considerable interest for super-resolution imaging [43] and enhanced optical sensing, communication, and inspection [44–46] due to their

unique intensity structures. Recently, by considering conservation of OAM in HHG upconversion, additional routes for controlling the OAM and polarization, as well as the spectral and temporal properties of HHG have been revealed [47–54]. A property particularly interesting for ptychography is the relationship between OAM and the HHG beam divergence/propagation: the spiral phase structure characteristic of OAM-HHG beams forces them to diverge more quickly from the focal point [53]. This means that, by using one or more OAM beams to drive the HHG process (referred to as OAM-HHG), one can control the divergence of the emitted HHG probe without changing the focusing optics of the HHG driving laser.

In this paper, we demonstrate a solution to a decade-long challenge by showing that high harmonic beams carrying orbital angular momentum can be used to advantage high-resolution, high-fidelity, and fast-convergence ptychographic imaging of highly periodic two-dimensional (2D) grating structures, using the standard extended ptychographic iterative engine (ePIE) algorithm [13]. The key to this technique is that the increased divergence of the OAM-HHG source, combined with the ring-shaped intensity distribution, introduces strong interference fringes between adjacent diffraction orders in the far-field. These encode the non-measurable phase information into the measurable intensity modulation in diffraction fields, significantly enhancing data diversity so that the phase of the diffracted field can be reliably retrieved. We further show that using OAM-HHG beams for illumination provides three significant advantages compared to standard Gaussian-HHG beams, all of which lead to enhanced signal-to-noise-ratio (SNR) for imaging periodic structures: First, due to the conservation of OAM in the HHG process and the resulting strong spiral phase structure in the generated EUV beams, OAM-HHG beams naturally have a significantly increased divergence compared to that of Gaussian-HHG beams. This enhanced illumination NA makes it possible to achieve overlap between different diffraction orders for small pitch periodic samples, beyond what is possible with a Gaussian-HHG probe, and without making any changes to the focusing optics of the ptychographic EUV microscope. Second, the unique ring-shaped OAM beam intensity distribution, which is determined by the strong spiral phase structure in the EUV beams, leads to overlap between different diffraction orders in the high-intensity regions of the beam. And third, OAM-HHG also allows a higher total number of photons to be collected by the detector given a fixed detector dynamic range. Therefore, by leveraging OAM-HHG beams for ptychography, we successfully imaged highly periodic samples with substantially reduced gridding artifacts and reliably detected defects near the diffraction limit. This new structured-EUV HHG metrology technique can support the advancement of next-generation EUV lithography, nanoelectronics, photonic, and quantum devices.

2. METHODOLOGY

To date, imaging highly periodic structures has been extremely challenging for ptychography. In a conventional implementation of ptychography using a Gaussian EUV beam to illuminate highly periodic 2D structures [see Fig. 1(a)], the far-field diffraction patterns consist of many isolated diffraction orders, each of which is a copy of the far-field beam profile and is modulated by an envelope in both amplitude and phase. The zoomed-in green circle in Fig. 1(a) shows this characteristic behavior, with the white
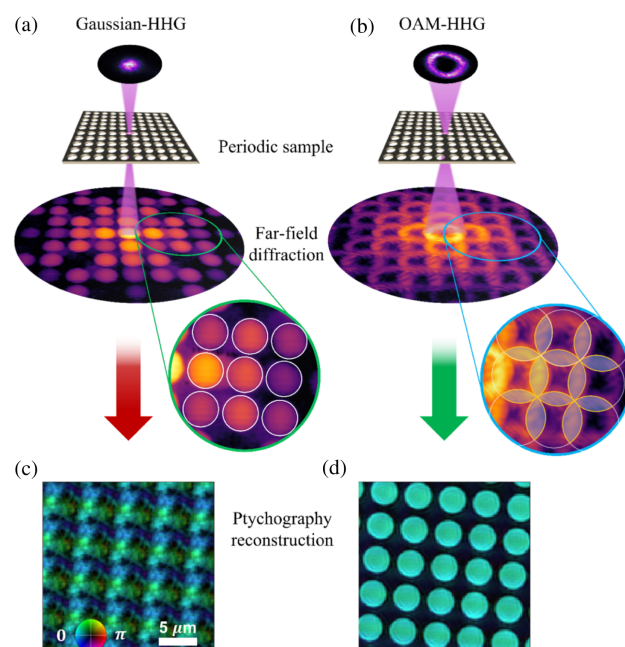

Fig. 1. Robust and reliable ptychographic imaging of highly periodic structures. (a) Schematic showing HHG ptychographic imaging of a periodic structure using conventional Gaussian-HHG illumination. The resulting diffraction orders are isolated (see zoomed-in green circle), where the white circles indicate the edges of each diffraction order. This leads to a complete loss of the relative phase information between the orders in the far-field diffraction, which subsequently leads to the failure of the ptychographic reconstruction in (b). (c) OAM-HHG illumination intrinsically has a larger source divergence and a ring-shaped intensity profile, to support overlap and interference between diffraction orders (see zoomed-in blue circle), in which the yellow circles indicate the edges of each diffraction order. This interference converts the relative phase between the diffraction orders into measurable intensity modulation, enabling fast and robust ptychographic reconstruction of the 2D periodic structure in (d). In (b), (d), the complex-valued amplitude and phase are plotted as brightness and hue, respectively.

circles indicating the edge of each diffraction order. In the resulting ptychographic dataset, diffraction patterns taken at different positions on the highly periodic sample are almost identical to each other. This is because, in contrast to diffraction from non-periodic structures, changes in the far-field diffraction field happen almost entirely in the relative phase between the diffraction orders, but not in the intensity (i.e., diffraction efficiency) of the diffracted orders. The phase information is, thus, totally lost in this case. Ptychography, as a phase retrieval algorithm, tries to retrieve the phase distributions of diffraction patterns from their intensity measurements. The fact that the phase information is totally lost for highly periodic samples with a sufficiently short period, as opposed to being encoded in the intensity measurements as would be the case for non-periodic structures, makes it extremely challenging to achieve successful ptychographic imaging of such highly periodic structures. As expected, the reconstruction fails for ptychography using a Gaussian-HHG beam, as shown in Fig. 1(b), in which the amplitude and phase of the reconstruction are plotted in brightness and hue, respectively. This phase problem can also be understood through the convolution theorem, as discussed in detail in Supplement 1, Section 1.

In 1969, Hoppe proposed to achieve electron diffraction imaging of periodic atomic lattices by encoding the non-measurable

phase information into the measurable intensity modulation in diffraction patterns through interference between neighboring diffraction orders [55]. As schematically shown in Fig. 1(c), OAM-HHG beams are able to achieve overlap and interference between neighboring diffraction orders due to their intrinsically larger beam divergence and ring-shaped intensity distribution. The zoomed-in blue circle in Fig. 1(c) shows the interference fringes, with the yellow circles indicating the edge of each diffraction order. As one scans the probe relative to the periodic structures, the relative phase of each diffraction order changes accordingly, which then causes the interference fringes to shift. In other words, the phase information in the diffraction patterns is now encoded in the intensity measurements through interference. These interference fringes contain the missing phase information and increase the diversity in diffraction patterns, thereby enabling robust and reliable ptychographic reconstructions (see Supplement 1, Section 3). Figure 1(d) shows a high-fidelity ptychographic reconstruction of a 2D periodic structure under an OAM-HHG illumination.

The required NA for high fidelity imaging of periodic samples can be understood as follows. When a periodic structure is illuminated by a focused coherent beam, the angular separation between two neighboring diffraction orders is given by $\Delta\theta = \lambda/\Lambda$, where λ is the illumination wavelength, and Λ is the period of the structure. The illumination NA for the microscope is defined as the half-cone angle of the focusing beam. Geometrically, for fixed λ and Λ, there exists a critical value for illumination NA,

$$\mathrm{NA}_c = \frac{1}{2}\Delta\theta = \frac{\lambda}{2\Lambda}. \qquad (1)$$

Only for illumination NAs larger than NA_c will neighboring diffraction orders have sufficiently large footprints on the detector to overlap with each other and generate interference fringes, thus enabling successful ptychographic reconstructions.

3. EXPERIMENTAL CONFIGURATION

We designed and built an EUV ptychographic microscope in a transmission geometry, as shown in Fig. 2. The driving laser for the HHG process is a frequency-doubled Ti:sapphire laser amplifier system ($\lambda \sim 395$ nm), with an intrinsic near-Gaussian

mode (vortex charge of $\ell = 0$), that can be converted to an OAM beam of vortex charge $\ell = 1$ using a spiral phase plate. The seventh harmonic of the driving laser ($\lambda \sim 56$ nm) exhibits either a Gaussian mode or an OAM of vortex charge $\ell = 7$ depending on whether a spiral phase plate is used. The EUV beam is then focused by a double-toroid focusing system onto the periodic samples, with a spot size of $\sim 13 \times 18$ μm ($1/e^2$ intensity) for Gaussian-mode HHG, or $\sim 27 \times 32$ μm (donut intensity peak-to-peak) for OAM-HHG. The reconstructed Gaussian- and OAM-HHG beam profiles are shown in a complex representation in Fig. S4 in Supplement 1, with the beam amplitude and phase indicated by brightness and hue. The test samples are three Quantifoil holey carbon films (~ 20 nm thick), which have various hole sizes and shapes arranged in a periodic rectangular grid. The three Quantifoil holey carbon films have a pitch of 9 μm, 4.5 μm, and 3 μm, respectively. These Quantifoil holey carbon films are mounted on standard Ted Pella ⌀3 mm Cu 200 mesh TEM grids. (See Section 2 for more information.)

During the ptychography scans, the test samples are translated in the plane perpendicular to the beam path in 7×7 rectangular grids (49 scan positions) with nominally 3.3 μm distance between adjacent scan positions. A random offset of $\pm 20\%$ of the scan step size was added to each scan position to avoid gridding artifacts in the reconstructions [56]. The far-field diffraction patterns are recorded by an EUV-CCD detector (Andor iKon-L, 2048×2048, 13.5 μm pixel size) positioned 50 mm after the sample. To obtain the best ptychographic reconstructions possible for each illumination case, we carefully pre-characterized each probe function in the sample plane by taking ptychographic scans on a non-periodic sample and reconstructing both the sample and the probe functions through blind deconvolution. These pre-characterized probe functions were used as initial guesses in the ptychographic reconstructions of highly periodic structures. Other than using the pre-characterized probe as the initial guess, we used the standard ePIE algorithm [13] for all reconstructions in this study, without the need for additional constraints such as the modulus enforced probe [15] or total variation regularization [25,57].
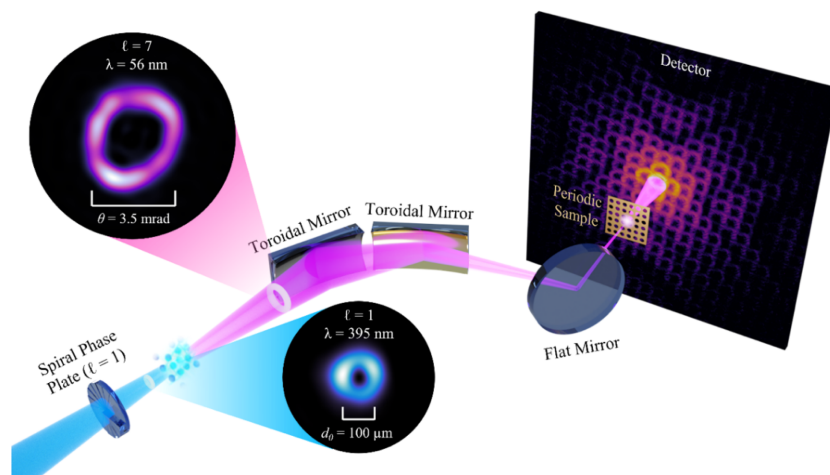

Fig. 2. EUV ptychographic microscope using OAM-HHG EUV beams for imaging highly periodic structures. A spiral phase plate ($\ell = 1$ at 395 nm wavelength) converts the driving laser at 395 nm wavelength to an OAM beam, which is focused into a semi-infinite gas cell to produce a nearly monochromatic seventh harmonic beam with a wavelength of 56 nm and an OAM charge of $\ell = 7$. A double-toroidal mirror focusing system focuses this OAM-HHG beam onto a 2D periodic sample, and an EUV-CCD camera is used to record the far-field diffraction patterns.
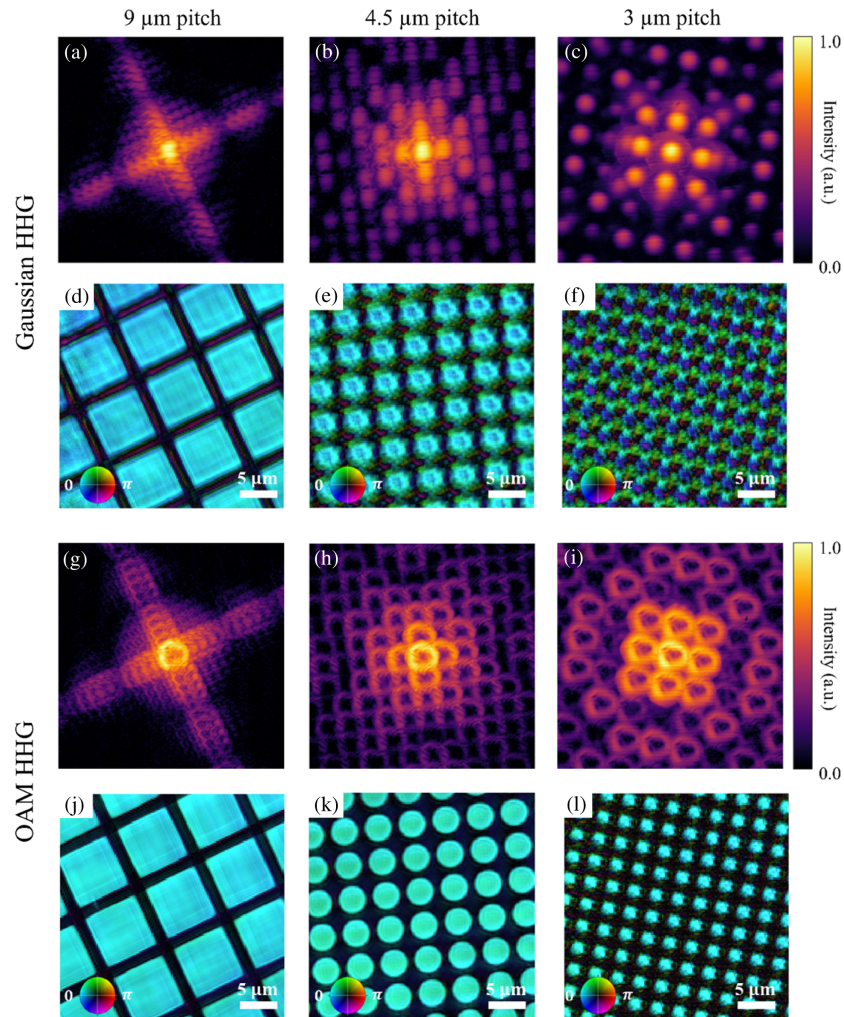
Fig. 3. High divergence OAM-HHG beams are able to produce higher-quality ptychography images of periodic structures than low divergence Gaussian-HHG beams. Three test samples with different periods and shapes, i.e., 9 μm period with square holes, 4.5 μm period with circular holes, and 3 μm period with circular holes, are investigated. For Gaussian-HHG beams, example diffraction patterns from the three test samples are shown in (a)–(c), and the corresponding ptychography reconstructed images are shown in (d)–(f). The example diffraction patterns and ptychography images from OAM-HHG beams are shown in (g)–(i) and (j)–(l). The complex-valued images in (d)–(f), (j)–(l) are plotted in a complex representation where amplitude and phase are shown in brightness and hue, respectively.

4. EXPERIMENTAL RESULTS

A. OAM-HHG Enables Robust and Reliable Ptychographic Imaging of Periodic Structures

We experimentally demonstrate that OAM-HHG beams enable robust and reliable ptychographic imaging of highly periodic structures because of three intrinsic advantages compared to Gaussian-HHG illumination. First, due to the conservation of OAM in the HHG process and the resulting strong spiral phase structure in the generated EUV beams, OAM-HHG beams naturally exhibit a significantly increased divergence (i.e., increased illumination NA for the microscope given the same focusing optics) compared with Gaussian-HHG beams. This enhanced illumination NA allows us to achieve overlap between diffraction orders for smaller pitch periodic samples beyond what is possible with a Gaussian-mode probe, without making any changes to the EUV microscope end-station. Second, the characteristic ring-shaped intensity distribution of OAM-HHG beams ensures that the majority of photons fall in the overlap area (in contrast to the Gaussian-HHG beams, for which the overlap between diffraction

orders occurs at the tails of the intensity distributions), which increases the SNR for the interference fringes. Third, the ring-shaped intensity distribution of OAM-HHG beams allows one to collect a higher total number of photons by the detector given a fixed dynamic range, which also leads to a higher SNR without the need for high dynamic range (HDR).

We performed ptychographic imaging on three highly periodic structures with 9 μm, 4.5 μm, and 3 μm pitches using Gaussian- and OAM-HHG beams at a wavelength of 56 nm. Using the same focusing optics, the effective illumination NA for these Gaussian-HHG and OAM-HHG beams is 0.062 and 0.14, respectively. Example diffraction patterns and reconstructed images from each ptychography scan can be found in Fig. 3. Furthermore, each ptychography scan collected 49 far-field diffraction intensity patterns, as shown in a log scale in Visualization 1. Note that, while there is a clear change in the diffraction patterns from frame to frame for the OAM-HHG case, particularly in the interference fringes between the adjacent diffraction orders, the diffraction patterns in the Gaussian-HHG case do not change very much for small period

samples. All ptychography datasets were taken without making any changes to the EUV microscope—the difference in divergence between Gaussian- and OAM-HHG beams is intrinsic to the HHG upconversion process, which conserves energy and OAM.

For the 9 μm pitch sample, the small diffraction angle means that successive orders largely overlap even for the Gaussian-HHG beam, as shown in Fig. 3(a). This results in a reasonably good image, apart from some gridding artifacts as shown in Fig. 3(d). In comparison, the ptychography scan using OAM-HHG illumination sees more overlap resulting in improved SNR in the interference fringes and a much higher-fidelity image with greatly reduced gridding artifacts, as shown in Figs. 3(g) and 3(j).

For the smaller 4.5 μm pitch sample, the diffraction orders are further apart, causing the Gaussian-HHG beams to lose most of the interference in the diffraction patterns, as shown in Fig. 3(b). The low SNR in the interference fringes results in reduced quality image reconstruction, as shown in Fig. 3(e). However, due to their higher intrinsic divergence and the unique ring-shaped intensity distribution, OAM-HHG maintains a large area of overlap between neighboring diffraction orders with more photons, as shown in Fig. 3(h). This results in higher-quality images of the periodic structure with a 4.5 μm period, as shown in Fig. 3(k). Thus, simply by inserting a spiral phase plate to convert the driving laser to an OAM beam, while keeping everything else in the microscope the same, a greatly improved reconstruction quality is obtained.

Lastly, for the smallest 3 μm period sample, Gaussian-HHG illumination totally fails due to the lack of interference between diffraction orders, as shown in Figs. 3(c) and 3(f). In this case, OAM beams can reconstruct a reasonable image, although the quality of the unit cell is degraded, as shown in Figs. 3(i) and 3(l).

We also evaluated the quality of these ptychographic reconstructions using complex histogram analysis, and the results can be found in Supplement 1, Section 4. We note that all reconstructions in Fig. 3 have the correct sample periodicity because this information is directly available from the measured intensity of the diffracted fields—the success or failure of the reconstructions of the unit cells depends on whether the relative phase between the diffraction orders can be successfully retrieved or not. The ptychography reconstructed images in Figs. 3(d)–3(f), 3(j)–3(l) are complex-valued and are shown in a complex representation where the amplitude and phase information are represented by the brightness and hue, respectively. The color wheel is shown in the bottom left corner of each panel.

B. OAM-HHG Beams Reveal Nanoscale Defects in Otherwise Periodic Samples

A major motivation for imaging periodic structures is to reliably detect and pinpoint small areas where the periodicity is broken, i.e., to locate defects. However, when the diffraction orders are insufficiently overlapped, the artifacts in the ptychographic reconstructions make it difficult or even impossible to locate defects. In contrast, the increase in reconstruction quality enabled by OAM-HHG beams, especially the suppression of periodic artifacts in the reconstructions (inherent to ptychographic imaging of periodic structures), enables reliable location of nanoscale defects in otherwise highly periodic structures. This can potentially find its application in metrology for micro- and nano-fabrication and manufacturing, including in advanced metrologies in support of EUV lithography.

In the 9 μm pitch sample, a damaged carbon bar (~300 nm wide) can be seen in the scanning electron microscopy (SEM) image in Fig. 4(e), indicated by the red arrow. We first performed ptychographic imaging of the corresponding area of the sample using an OAM-HHG beam. During data acquisition at each scan position, we acquired two diffraction patterns with exposure times of 0.1 and 1 s, and we combined them to form a composite high dynamic range (HDR) image to increase SNR. The reconstructed image of the transmitted amplitude is shown in Fig. 4(a), in which the defect is clearly resolved and is indicated by the red arrow. Given that the pixel size in the ptychography reconstruction images is 200 nm, the fact that our EUV microscope using OAM-HHG illuminations can clearly image a defect with size of about 300 nm (i.e., $1.5\times$ the pixel size in the reconstruction images) makes it very promising to detect or image smaller defects down to 10 s of nanometers using shorter EUV wavelengths and increased imaging NA.

Next, a similar experiment is performed using a Gaussian-HHG beam under the same conditions, resulting in the same approximate maximum detector count in the diffraction patterns as for the OAM case. The reconstructed image of the transmitted amplitude is shown in Fig. 4(b), where reconstruction artifacts heavily corrupt the image details and render the defect unidentifiable. Furthermore, due to the different intensity distributions of the Gaussian- and OAM-HHG beams, even though the two datasets have the same maximum detector count, the OAM dataset has 3 times more total detector counts than the Gaussian one.

To confirm that the difference in reconstructed image quality is not simply due to this different in the total number of photons collected, but is due to how those photons are distributed in the diffraction plane (i.e., in the area of overlap between diffraction orders), we performed a third experiment using the Gaussian-HHG beam and triple HDR exposure (0.1, 1, and 3 s exposure time), which leads to longer data acquisition time by a factor of 1.67, to have approximately equal total counts in the combined diffraction data compared to the OAM-HHG case. The resulting amplitude image is shown in Fig. 4(c). There is significant improvement over the reconstructed image from Gaussian-HHG beams with double HDR exposure, but the reconstruction artifacts still make it difficult to identify the nanoscale defect. We further quantitatively analyzed the SNR of the defect in these three reconstruction amplitude images using the transmission profiles of the thin carbon bar in the boxes in Figs. 4(a)–4(c). These transmission profiles are obtained by averaging the transmission images in the vertical direction and are plotted along the horizontal direction, as shown in Fig. 4(d). The SNRs of the defect in Figs. 4(a)–4(c) are calculated (see Section 2) and summarized in Table 1. The SNR for the defect image from OAM-HHG illumination is improved by a factor of >135 compared to that from Gaussian-HHG illumination with equal exposure time. Furthermore, we evaluated the quality of these ptychographic reconstructions using complex histogram analysis and verified that OAM-HHG illuminations result in higher fidelity images, as discussed in detail in Supplement 1, Section 4. It is worth emphasizing that, when taking the SEM image in Fig. 4(e), the high-energy electron beam at 3 keV severely damaged the thin carbon bar, causing shrinkage and the appearance of the bright areas on the top and bottom edges. In contrast, the EUV HHG beam can non-destructively image both the periodic sample and the defect.
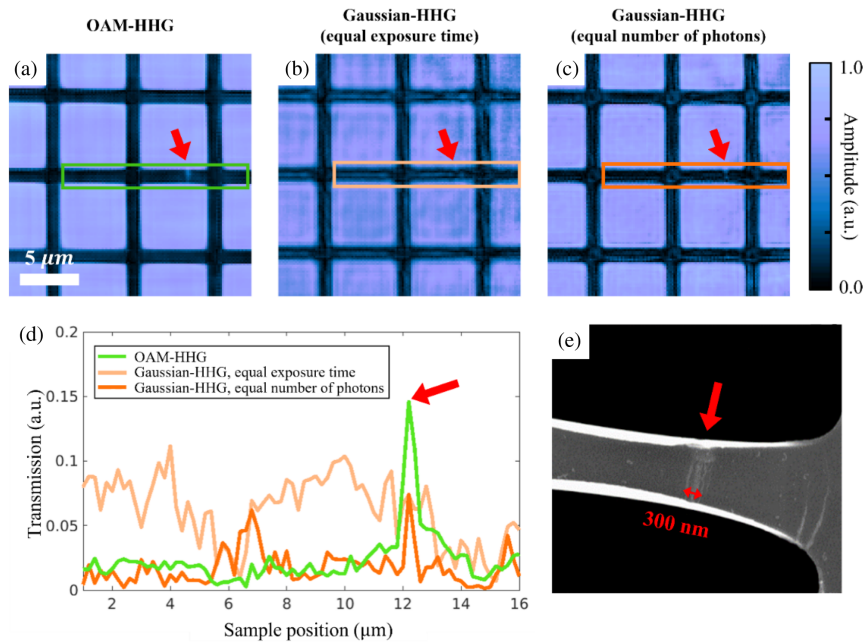
Fig. 4. Enhanced sensitivity to nanoscale defects in periodic structures using OAM-HHG beams. (a)–(c) Amplitude images of ptychographic reconstruction of a 2D square periodic structure (9 μm period, with a nanoscale defect of ∼300 nm in size) under various conditions: (a) OAM-HHG beams with double HDR (0.1 and 1 s exposure times), (b) Gaussian-HHG beams with equal exposure time as the OAM-HHG case using double HDR (0.1 and 1 s exposure times), and (c) Gaussian-HHG beams with roughly equal number of photons as the OAM-HHG case using triple HDR (0.1, 1, and 3 s exposure times). The red arrows indicate the nano-defect in the thin carbon bar. (d) Ptychography reconstructed transmission profile of the thin carbon bar containing a nano-defect (indicated by the red arrow) in the boxes in (a)–(c). The transmission profiles are averaged in the vertical direction. The red arrow indicates the nano-defect. (e) An SEM image of the same sample area shows a 300-nm-wide defect. Bright areas on the top and bottom edges are due to sample damage from the high energy electron (3 keV) beams.

Table 1. Signal-to-Noise Ratio Analysis for the Three Ptychographic Reconstructions Shown in Figs. 4(a)–4(c)

Ptychographic Reconstructions	Signal	Background	Noise	SNR	Improvement Factor
OAM-HHG in Fig. 4(a)	1.46e-1	1.52e-2	5.62e-3	23.3	**137**
Gaussian-HHG, equal exposure time in Fig. 4(b)	7.34e-2	6.94e-2	2.35e-2	0.170	Benchmark
Gaussian-HHG, equal number of photons in Fig. 4(c)	7.40e-2	1.72e-2	1.31e-2	4.34	25.5

5. CONCLUSION

In conclusion, we demonstrated that, by incorporating illumination engineering via OAM-HHG beams into an EUV ptychography microscope, we can address the long-standing challenge of high-fidelity coherent diffractive imaging of periodic structures. The intrinsic large divergence and ring-shaped intensity distribution of OAM-HHG beams leads to the formation of higher SNR interference fringes in the diffraction patterns—thus enabling faster and higher fidelity image reconstructions using the basic ePIE algorithm, without extra algorithmic effort. Furthermore, the improvement in image fidelity allowed sensitive detection of a 300 nm wide defect, which is 1.5× the pixel size of the reconstructed images, in an otherwise periodic thin carbon mesh with 9 μm period.

Ptychographic imaging of highly periodic structures has been widely recognized to be challenging, which has precluded its application in critical science and technology fields such as semiconductor metrology and EUV photomask inspection. Future studies can employ coherent EUV and x-ray vortex beams to enable nanometer- or even sub-nanometer-scale spatial resolution in a broad range of next-generation nanoelectronics, photonics, and quantum devices. A particularly interesting direction would be to use coherent EUV light at a wavelength of 13.5 nm for actinic imaging and inspection of EUV photomasks [19–25]. Finally, this work can provide inspiration for the electron ptychography community (e.g., cryo-EM and 4D-STEM), where recent work has explored the potential benefits of engineered vortex electron beams for enhanced imaging fidelity and lower dose [58,59].

Supplemental document. See Supplement 1 for supporting content.

REFERENCES

1. J. Miao, P. Charalambous, and D. Sayre, "Extending the methodology of X-ray crystallography to allow imaging of micrometer-sized non-crystalline specimens," Nature **400**, 342–344 (1999).
2. J. M. Rodenburg, A. C. Hurst, A. G. Cullis, *et al.*, "Hard-X-ray lensless imaging of extended objects," Phys. Rev. Lett. **98**, 034801 (2007).
3. J. M. Rodenburg, A. C. Hurst, and A. G. Cullis, "Transmission microscopy without lenses for objects of unlimited size," Ultramicroscopy **107**, 227–231 (2007).
4. P. Thibault, M. Dierolf, A. Menzel, *et al.*, "High-resolution scanning x-ray diffraction microscopy," Science **321**, 379–382 (2008).
5. M. D. Seaberg, B. Zhang, D. F. Gardner, *et al.*, "Tabletop nanometer extreme ultraviolet imaging in an extended reflection mode using coherent Fresnel ptychography," Optica **1**, 39–44 (2014).
6. D. A. Shapiro, Y.-S. Yu, T. Tyliszczak, *et al.*, "Chemical composition mapping with nanometre resolution by soft X-ray microscopy," Nat. Photonics **8**, 765–769 (2014).
7. C. Donnelly, M. Guizar-Sicairos, V. Scagnoli, *et al.*, "Element-specific X-ray phase tomography of 3D structures at the nanoscale," Phys. Rev. Lett. **114**, 115501 (2015).
8. Y. H. Lo, C.-T. Liao, J. Zhou, *et al.*, "Multimodal X-ray and electron microscopy of the Allende meteorite," Sci. Adv. **5**, eaax3009 (2019).
9. M. Tanksalvala, C. L. Porter, Y. Esashi, *et al.*, "Nondestructive, high-resolution, chemically specific 3D nanostructure characterization using phase-sensitive EUV imaging reflectometry," Sci. Adv. **7**, eabd9667 (2021).
10. L. Loetgering, S. Witten, and J. Rothhardt, "Advances in laboratory-scale ptychography using high harmonic sources," Opt. Express **30**, 4133–4164 (2022).
11. J. R. Fienup, "Phase retrieval algorithms: a comparison," Appl. Opt. **21**, 2758–2769 (1982).
12. D. R. Luke, "Relaxed average alternating reflections for diffraction imaging," Inverse Prob. **21**, 37–50 (2005).
13. A. M. Maiden and J. M. Rodenburg, "An improved ptychographical phase retrieval algorithm for diffractive imaging," Ultramicroscopy **109**, 1256–1262 (2009).
14. P. Thibault and M. Guizar-Sicairos, "Maximum-likelihood refinement for coherent diffractive imaging," New J. Phys. **14**, 063004 (2012).
15. D. F. Gardner, M. Tanksalvala, E. R. Shanblatt, *et al.*, "Subwavelength coherent imaging of periodic samples using a 13.5 nm tabletop high-harmonic light source," Nat. Photonics **11**, 259–264 (2017).
16. S. Lazarev, I. Besedin, A. V. Zozulya, *et al.*, "Ptychographic X-ray imaging of colloidal crystals," Small **14**, 1702575 (2018).
17. G. F. Mancini, R. M. Karl, E. R. Shanblatt, *et al.*, "Colloidal crystal order and structure revealed by tabletop extreme ultraviolet scattering and coherent diffractive imaging," Opt. Express **26**, 11393–11406 (2018).
18. M. Holler, M. Guizar-Sicairos, E. H. R. Tsai, *et al.*, "High-resolution non-destructive three-dimensional imaging of integrated circuits," Nature **543**, 402–406 (2017).
19. T. Harada, M. Nakasuji, T. Kimura, *et al.*, "Imaging of extreme-ultraviolet mask patterns using coherent extreme-ultraviolet scatterometry microscopes based on coherent diffraction imaging," J. Vac. Sci. Technol. B **29**, 06F503 (2011).
20. K. A. Goldberg, I. Mochi, M. Benk, *et al.*, "Commissioning an EUV mask microscope for lithography generations reaching 8 nm," Proc. SPIE **8679**, 867919 (2013).
21. P. Helfenstein, I. Mohacsi, R. Rajendran, *et al.*, "Scanning coherent diffractive imaging methods for actinic EUV mask metrology," Proc. SPIE **9776**, 97761F (2016).
22. D. Hellweg, M. Koch, S. Perlitz, *et al.*, "Actinic review of EUV masks: performance data and status of the AIMS EUV system," Proc. SPIE **10143**, 101430J (2017).
23. R. Rajendran, I. Mochi, P. Helfenstein, *et al.*, "Towards a stand-alone high-throughput EUV actinic photomask inspection tool–RESCAN," Proc. SPIE **10145**, 101450N (2017).
24. I. Mochi, S. Fernandez, R. Nebling, *et al.*, "Quantitative characterization of absorber and phase defects on EUV reticles using coherent diffraction imaging," J. Micro/Nanolithogr. MEMS MOEMS **19**, 014002 (2020).
25. B. Wang, N. Brooks, M. Tanksalvala, *et al.*, "Robust and reliable actinic ptychographic imaging of highly periodic structures in EUV photomasks," Proc. SPIE **12293**, 122930N (2022).
26. A. Rundquist, C. G. Durfee, III, Z. Chang, *et al.*, "Phase-matched generation of coherent soft X-rays," Science **280**, 1412–1415 (1998).
27. R. A. Bartels, A. Paul, H. Green, *et al.*, "Generation of spatially coherent light at extreme ultraviolet wavelengths," Science **297**, 376–378 (2002).
28. X. Zhang, A. R. Libertun, A. Paul, *et al.*, "Highly coherent light at 13 nm generated by use of quasi-phase-matched high-harmonic generation," Opt. Lett. **29**, 1357–1359 (2004).
29. P. D. Baksh, M. Ostrčil, M. Miszczak, *et al.*, "Quantitative and correlative extreme ultraviolet coherent imaging of mouse hippocampal neurons at high resolution," Sci. Adv. **6**, eaaz3025 (2020).
30. N. J. Brooks, B. Wang, I. Binnie, *et al.*, "Temporal and spectral multiplexing for EUV multibeam ptychography with a high harmonic light source," Opt. Express **30**, 30331–30346 (2022).
31. W. Eschen, L. Loetgering, V. Schuster, *et al.*, "Material-specific high-resolution table-top extreme ultraviolet microscopy," Light Sci. Appl. **11**, 117 (2022).
32. T. Fan, P. Grychtol, R. Knut, *et al.*, "Bright circularly polarized soft X-ray high harmonics for X-ray magnetic circular dichroism," Proc. Natl. Acad. Sci. USA **112**, 14206–14211 (2015).
33. C. Chen, Z. Tao, C. Hernández-García, *et al.*, "Tomographic reconstruction of circularly polarized high harmonic fields: 3D attosecond metrology," Sci. Adv. **2**, e1501333 (2016).
34. D. Zusin, P. M. Tengdin, M. Gopalakrishnan, *et al.*, "Direct measurement of the static and transient magneto-optical permittivity of cobalt across the entire M-edge in a reflection geometry by use of polarization scanning," Phys. Rev. B **97**, 024433 (2018).
35. A. Rana, C.-T. Liao, E. Iacocca, *et al.*, "Three-dimensional topological magnetic monopoles and their interactions in a ferromagnetic meta-lattice," Nat. Nanotechnol. **18**, 227–232 (2023).
36. A. M. Maiden, M. J. Humphry, F. Zhang, *et al.*, "Superresolution imaging via ptychography," J. Opt. Soc. Am. A **28**, 604–612 (2011).
37. M. Guizar-Sicairos, M. Holler, A. Diaz, *et al.*, "Role of the illumination spatial-frequency spectrum for ptychography," Phys. Rev. B **86**, 100103 (2012).
38. A. Fannjiang and W. Liao, "Phase retrieval with random phase illumination," J. Opt. Soc. Am. A **29**, 1847–1859 (2012).
39. A. M. Maiden, G. R. Morrison, B. Kaulich, *et al.*, "Soft X-ray spectromicroscopy using ptychography with randomly phased illumination," Nat. Commun. **4**, 1669 (2013).
40. T. B. Edo, D. J. Batey, A. M. Maiden, *et al.*, "Sampling in X-ray ptychography," Phys. Rev. A **87**, 053850 (2013).
41. N. Burdet, G. R. Morrison, X. Huang, *et al.*, "Observations of artefacts in the X-ray ptychography method," Opt. Express **22**, 10294–10303 (2014).
42. M. Odstrčil, M. Lebugle, M. Guizar-Sicairos, *et al.*, "Towards optimized illumination for high-resolution ptychography," Opt. Express **27**, 14981–14997 (2019).
43. E. Betzig, G. H. Patterson, R. Sougrat, *et al.*, "Imaging intracellular fluorescent proteins at nanometer resolution," Science **313**, 1642–1645 (2006).
44. J. P. Torres and L. Torner, *Twisted Photons: Applications of Light with Orbital Angular Momentum* (Wiley, 2011).
45. A. E. Willner, H. Huang, Y. Yan, *et al.*, "Optical communication using orbital angular momentum beams," Adv. Opt. Photon. **7**, 66–106 (2015).
46. B. Wang, M. Tanksalvala, Z. Zhang, *et al.*, "Coherent Fourier scatterometry using orbital angular momentum beams for defect detection," Opt. Express **29**, 3342–3358 (2021).
47. C. Hernández-García, A. Picón, J. S. Román, *et al.*, "Attosecond extreme ultraviolet vortices from high-order harmonic generation," Phys. Rev. Lett. **111**, 083602 (2013).
48. G. Gariepy, J. Leach, K. T. Kim, *et al.*, "Creating high-harmonic beams with controlled orbital angular momentum," Phys. Rev. Lett. **113**, 153901 (2014).

49. R. Géneaux, A. Camper, T. Auguste, *et al.*, "Synthesis and characterization of attosecond light vortices in the extreme ultraviolet," Nat. Commun. **7**, 12583 (2016).

50. K. M. Dorney, L. Rego, N. J. Brooks, *et al.*, "Controlling the polarization and vortex charge of attosecond high-harmonic beams via simultaneous spin–orbit momentum conservation," Nat. Photonics **13**, 123–130 (2019).

51. W. Paufler, B. Böning, and S. Fritzsche, "High harmonic generation with Laguerre-Gaussian beams," J. Opt. **21**, 094001 (2019).

52. L. Rego, K. M. Dorney, N. J. Brooks, *et al.*, "Generation of extreme-ultraviolet beams with time-varying orbital angular momentum," Science **364**, eaaw9486 (2019).

53. L. Rego, N. J. Brooks, Q. L. D. Nguyen, *et al.*, "Necklace-structured high-harmonic generation for low-divergence, soft X-ray harmonic combs with tunable line spacing," Sci. Adv. **8**, eabj7380 (2022).

54. F. Kong, C. Zhang, F. Bouchard, *et al.*, "Controlling the orbital angular momentum of high harmonic vortices," Nat. Commun. **8**, 14970 (2017).

55. W. Hoppe, "Diffraction in inhomogeneous primary wave fields. I. Principle of phase determination from electron diffraction interference," Acta Crystallogr. A **25**, 495–501 (1969).

56. P. Thibault, M. Dierolf, O. Bunk, *et al.*, "Probe retrieval in ptychographic coherent diffractive imaging," Ultramicroscopy **109**, 338–343 (2009).

57. R. Nebling, I. Mochi, H.-S. Kim, *et al.*, "A priori information in ptychographic image reconstruction for EUV mask metrology," Proc. SPIE **11875**, 118750M (2021).

58. P. M. Pelz, W. X. Qiu, R. Bücker, *et al.*, "Low-dose cryo electron ptychography via non-convex Bayesian optimization," Sci. Rep. **7**, 9883 (2017).

59. S. E. Zeltmann, A. Müller, K. C. Bustillo, *et al.*, "Patterned probes for high precision 4D-STEM Bragg measurements," Ultramicroscopy **209**, 112890 (2020).